

References and Notes

- G. C. Nanson, D. M. Price, S. A. Short, *Geology* **20**, 791 (1992); J. Croke, J. Magee, D. Price, *Palaeogeogr. Palaeoclimatol. Palaeoecol.* **124**, 1 (1996); J. M. Bowler and R. J. Wasson, in *Late Cainozoic Paleoclimates of the Southern Hemisphere*, J. C. Vogel, Ed. (Balkema, Rotterdam, 1984), pp. 183–208; J. M. Bowler, in *Evolution of the Flora and Fauna of Arid Australia*, W. R. Barker and P. J. M. Greenslade, Eds. (Peacock Publications, Frewville, SA, Australia, 1982), pp. 35–45; R. J. Wasson, *Geogr. Rev. Jpn. Ser. B* **59**, 55 (1986).
- J. W. Magee, J. M. Bowler, G. H. Miller, D. L. G. Williams, *Palaeogeogr. Palaeoclimatol. Palaeoecol.* **113**, 3 (1995); J. W. Magee, thesis, Australian National University, Canberra (1997); — and G. H. Miller, *Palaeogeogr. Palaeoclimatol. Palaeoecol.* **144**, 307 (1998).
- S. Pearson and J. R. Dodson, *Quat. Res.* **39**, 347 (1993); L. McCarthy, L. Head, J. Quade, *Palaeogeogr. Palaeoclimatol. Palaeoecol.* **123**, 205 (1996); J. G. Luly, *J. Biogeogr.* **20**, 587 (1993).
- G. Singh and J. Luly, *Palaeogeogr. Palaeoclimatol. Palaeoecol.* **84**, 75 (1991).
- R. G. Roberts, R. Jones, M. A. Smith, *Nature* **345**, 153 (1990); R. G. Roberts et al., *Quat. Sci. Rev.* **13**, 575 (1994).
- G. H. Miller et al., *Science* **283**, 205 (1999).
- Isotopic data are reported in δ values, where $\delta^{13}\text{C}$ (in per mil) = $[(^{13}\text{C}/^{12}\text{C})_{\text{sample}} / (^{13}\text{C}/^{12}\text{C})_{\text{standard}} - 1] \times 1000$, and the isotopic standard is Vienna Pee Dee belemnite, calibrated through National Bureau of Standards reference materials.
- K. A. Hobson, *Condor* **97**, 752 (1995).
- Y. von Schirnding, N. J. Van der Merwe, J. C. Vogel, *Archaeometry* **24**, 3 (1982); B. J. Johnson, M. L. Fogel, G. H. Miller, *Geochim. Cosmochim. Acta* **62**, 2451 (1998).
- C. L. Coddington, thesis, Australian National University, Canberra (1992).
- S. J. F. Davies, *Aust. J. Ecol.* **3**, 411 (1978); T. J. Dawson, D. Read, E. M. Russell, R. M. Herd, *Emu* **84**, 93 (1984).
- P. W. Hattersley, *Oecologia* **57**, 113 (1983).
- N. Nicholls, *Vegetatio* **91**, 23 (1991).
- B. N. Smith and S. Epstein, *Plant Physiol.* **47**, 380 (1971).
- The fossil eggshells were dated by direct accelerator mass spectrometry (AMS) ^{14}C ($n = 77$) and from the extent of amino acid racemization [D-alloisoleucine/L-isoleucine (D/L); $n = 219$]. For those samples not directly dated by AMS ^{14}C , we used the age model of Miller et al. (6) to assign ages to each D/L value. Errors in converting D/L to age are primarily related to the depth of burial and the low rate of racemization during the cold interval between 15 and 40 ka (27). Comparing ^{14}C -D/L model-age pairs between 0 and 14.5 ka, we found that the average error is 1600 years. For the period between 14.5 and 36 ka, ^{14}C -D/L model age pairs have an average error of 7900 years because temperatures were low and most LGM deposits are <2 m thick. We cannot formally evaluate the error for older samples, but because the deposits are much thicker (>4 m) and temperatures were warmer, the model-age error should be less.
- For isotopic analyses of the EES calcite, between 2 and 3 mg of ground EES were reacted with 100% H_3PO_4 at 60°C, and the resultant CO_2 was analyzed with a Finnigan MAT 252 mass spectrometer (Geophysical Laboratory), or between 100 and 150 mg of ground EES were reacted with 105% H_3PO_4 at 90°C with an automated individual carbonate reaction Kiel device coupled with a Finnigan MAT 251 mass spectrometer (Research School of Earth Sciences). The carbon isotopic offset between the inorganic and total organic fractions of EES (as defined by $\Delta^{13}\text{C} = \delta^{13}\text{C}_{\text{inorg}} - \delta^{13}\text{C}_{\text{org}}$) was used as a means to evaluate the amount of isotopic exchange that occurred in the fossil samples. The average $\Delta^{13}\text{C}$ of modern EES was 9.0 ± 1.0 per mil ($n = 37$), regardless of the $\delta^{13}\text{C}$ value of the diet (Web Table 1), and the average $\Delta^{13}\text{C}$ of fossil EES was 10.4 ± 2.0 per mil ($n = 45$) (Web Table 2). The general agreement between the $\Delta^{13}\text{C}$ values of modern and fossil EES implies excellent preservation of both eggshell fractions through geologic time; however, seven EESs with $\Delta^{13}\text{C}$ values greater than $\pm 2\sigma$ from the average modern $\Delta^{13}\text{C}$ value were excluded from the data analysis (Web Table 2).
- P. Latz, *Bushfires and Bushtucker* (Institute for Aboriginal Development Press, Alice Springs, NT, Australia, 1995).
- A.-M. Aucour et al., *Quat. Res.* **41**, 224 (1994); F. A. Street-Perrott et al., *Science* **278**, 1422 (1997).
- B. Liu, F. M. Phillips, A. R. Cambell, *Palaeogeogr. Palaeoclimatol. Palaeoecol.* **124**, 233 (1996); S. L. Connin, J. Betancourt, J. Quade, *Quat. Res.* **50**, 179 (1998).
- J. M. Barnola, D. Raynaud, Y. S. Korotkevich, C. Lorius, *Nature* **329**, 408 (1987).
- G. H. Miller, J. W. Magee, A. J. T. Jull, *ibid.* **385**, 241 (1997).
- T. E. Cerling et al., *ibid.* **389**, 153 (1997).
- B. D. Marino and M. B. McElroy, *ibid.* **349**, 127 (1991).
- J. C. Noble, *The Delicate and Noxious Scrub* (Commonwealth Scientific and Industrial Research Organisation, Canberra, 1997); D. A. Adamson and M. D. Fox, in *A History of Australian Vegetation*, J. M. B. Smith, Ed. (McGraw-Hill, Sydney, 1982), pp. 109–146.
- T. Flannery, *The Future Eaters* (Reed Books, Melbourne, 1994).
- A. P. Kershaw, *Nature* **322**, 47 (1986); G. Singh and E. A. Geissler, *Philos. Trans. R. Soc. London Ser. B* **311**, 379 (1985).
- W. L. Prell and J. E. Kutzbach, *J. Geophys. Res.* **92**, 8411 (1987); Z. An, G. J. Kukla, S. C. Porter, J. Xiao, *Quat. Res.* **36**, 29 (1991); J. L. Xiao et al., *Quat. Sci. Rev.* **18**, 147 (1999).
- A. Henderson-Sellers et al., *J. Geophys. Res.* **98**, 7289 (1993); J. Kutzbach, G. Bonan, J. Foley, S. P. Harrison, *Nature* **384**, 623 (1996).
- G. H. Miller and J. W. Magee, *Eos Trans. Am. Geophys. Union Fall Meet. Suppl.* **73** (no. 43), 104 (1992).
- N. J. Tapper and L. Hurry, *Australia's Weather Patterns: An Introductory Guide* (Dellasta, Mount Waverley, VIC, Australia, 1993); J. Gentili, Ed., in *Climates of Australia and New Zealand*, (Elsevier, Amsterdam, 1971), pp. 53–117.
- Mean monthly precipitation values at meteorological stations closest to the eggshell collection sites were provided by the Commonwealth Bureau of Meteorology, Melbourne (available at www.bom.gov.au/climate/averages).
- The ratio of C_3 to C_4 plants in emu diets was calculated from $\delta^{13}\text{C}_{\text{EES}}$ values using a two-end-member mixing model as follows:

$$\delta^{13}\text{C}_{\text{EES}} - \text{BF} = \delta^{13}\text{C}_{\text{C}_3}(\text{X}) + \delta^{13}\text{C}_{\text{C}_4}(1 - \text{X}),$$
 where BF is biochemical fractionation (10 per mil for EES calcite), $\delta^{13}\text{C}_{\text{C}_3} = -26.5$ per mil, $\delta^{13}\text{C}_{\text{C}_4} = -12.5$ per mil, and X is the proportion of C_3 plants in the diet. The variability associated with the BF and the isotopic compositions of the end-members corresponds to an uncertainty of $\pm 15\%$ in the C_3/C_4 dietary calculations; thus, these calculations are primarily useful for comparative purposes.
- This research was funded by the International Programs Division (B.J.J.) and the Division of Atmospheric Science of NSF (B.J.J., G.H.M., and M.L.F.), the Geophysical Laboratory at the Carnegie Institution of Washington, and the Australian National University. We thank G. Atkin, S. Webb, O. Miller, and P. Clark for assistance in obtaining samples; C. Hart and J. Cali for laboratory assistance; and P. Koch, J. Luly, M. Duvall, K. Hughen, M. Teece, V. Sloan, and J. Brandes for comments on early drafts of the manuscript.

14 January 1999; accepted 9 April 1999

Electrostatic Modulation of Superconductivity in Ultrathin GdBa₂Cu₃O_{7-x} Films

C. H. Ahn, S. Gariglio, P. Paruch, T. Tybell, L. Antognazza, J.-M. Triscone

The polarization field of the ferroelectric oxide lead zirconate titanate [Pb(Zr_xTi_{1-x})O₃] was used to tune the critical temperature of the high-temperature superconducting cuprate gadolinium barium copper oxide (GdBa₂Cu₃O_{7-x}) in a reversible, nonvolatile fashion. For slightly underdoped samples, a uniform shift of several Kelvin in the critical temperature was observed, whereas for more underdoped samples, an insulating state was induced. This transition from superconducting to insulating behavior does not involve chemical or crystalline modification of the material.

Superconductor-insulator transitions have been investigated theoretically and experimentally in a variety of systems, including three-dimensional (3D) ionic crystals, 2D films, and Josephson junction arrays. These transitions are examples of the modulation of superconductivity by means of control parameters such as pressure, magnetic field, disorder, and thickness (1–4). For applications, superconducting bolometers operate on changes in the temperature, and superconducting quantum interference de-

vices rely on the application of small magnetic fields that modulate the critical current of a Josephson junction.

Here we report on nonvolatile, reversible modulation of superconductivity in the high-temperature copper oxide superconductor GdBa₂Cu₃O_{7-x} (GBCO), using an electrostatic field as the control parameter. A unique feature of these cuprate materials, as compared to the elemental BCS superconductors, is that their properties depend strongly on the carrier concentration, as shown by their generic temperature-doping phase diagram (Fig. 1), which depicts an antiferromagnetic insulating state at low doping levels that is

Département de Physique de la Matière Condensée, University of Geneva, 24 Quai Ernest-Ansermet, 1211 Geneva 4, Switzerland.

separated from a superconducting state at higher doping levels. This phase diagram suggests, in the underdoped regime, a superconductor-insulator quantum phase transition controlled solely by the doping level (or chemical potential), as outlined in the recent SO(5) theory of Zhang (5).

In our experiment, we controlled the doping level using the polarization field of a ferroelectric oxide, $\text{Pb}(\text{Zr}_x\text{Ti}_{1-x})\text{O}_3$ (PZT), grown epitaxially on ultrathin films of GBCO, to change the carrier concentration and modulate the electronic properties of the superconducting layer without introducing any chemical or microscopic structural disorder. This approach is both reversible and nonvolatile, with no external electric field being applied across the insulating ferroelectric during the measurement of the properties of the superconducting layer (6).

The field effect has been used before to shift the critical temperature of elemental superconductors by ~ 1 mK (7). It has also been applied to the copper oxide superconductors to shift the critical temperature by a few kelvin, as well as to study vortex dynamics by changing the effective thickness of the superconductor (8). In these studies, the volume and number of charge carriers were too substantial to change the metallic character of the superconductor. On the applied side, proximity field-effect devices and Josephson field-effect transistors have been fabricated (9). For all of these studies, a conventional field-effect device, in which a continuous voltage is applied across the gate insulator, was used.

To grow the PZT/GBCO heterostructures, we carried out off-axis radio frequency magnetron sputtering onto single crystalline SrTiO_3 (STO) (001) substrates, a process that is described in detail elsewhere (10). Because the carrier density of the copper oxide superconductors is relatively large, $\sim 10^{21}/\text{cm}^3$, the electrostatic Thomas-Fermi screening length is on the order of a few angstroms, which necessitates the use of extremely thin GBCO layers, ~ 1 to 2 unit cells thick (12 to 24 Å), in order to obtain substantial field effects. To grow such thin layers, a buffer layer of insulating (at low temperature) $\text{PrBa}_2\text{Cu}_3\text{O}_7$ (PBCO), 72 Å thick, was first grown on the STO substrate, as has been used previously for the growth of ultrathin $\text{YBa}_2\text{Cu}_3\text{O}_{7-x}$ films and multilayers (11). X-ray diffraction revealed epitaxial growth of PZT (001), GBCO (001), and PBCO (001) on STO (001) substrates (12). For (001)-oriented PZT, the two ferroelectric polarization states lie perpendicular to the GBCO layer, and Sawyer-Tower measurements on these samples reveal a remnant polarization of $\sim 10 \mu\text{C}/\text{cm}^2$ and a coercive field of 100 kV/cm. The heterostructures were then patterned into four point resistivity paths, with Au pads being deposited for the current and voltage contacts, as well as for the poling contact on top of the PZT layer.

We first examined the ferroelectric field effect in these PZT/GBCO heterostructures by measuring their room-temperature resistance as a function of the poling field used to establish the polarization state of the ferroelectric layer. A voltage pulse (~ 1 s) was applied across the ferroelectric, after which the resistance was measured. By repeating this procedure for a series of different voltages, the ferroelectric hysteresis [resistance versus field (R-E)] was revealed (Fig. 2) for a 3000 Å PZT/ 20 Å GBCO/72 Å PBCO heterostructure. The measured coercive field was 100 kV/cm, and the difference in resistance of the GBCO/PBCO bilayer between the two polarization states of PZT was $\sim 10\%$, with the sign of the resistance change agreeing with the hole-doped character of GBCO. The resistance states after application of the voltage pulses were nonvolatile for periods of hours (the length of the experiments) and were also reversible, as demonstrated by the hysteresis. For comparison, we show in the inset to Fig. 2 a ferroelectric hysteresis loop [polarization versus field (P-E)] obtained through a standard Sawyer-Tower measurement on this sample, showing a coercive field of 100 kV/cm and a remnant polarization of $10 \mu\text{C}/\text{cm}^2$. Although the coercive fields of both measurements agree, extracting a quantitative value for the remnant polarization is not straightforward from the R-E measurement, because the resistance change does not directly reveal the magnitude of the ferroelectric polarization. A free electron estimate, however, based on assuming $d\sigma/\sigma \sim dn/n$, where σ is the conductivity of the GBCO/PBCO bilayer and n

is the carrier concentration, yields a value consistent with a polarization of $10 \mu\text{C}/\text{cm}^2$. The hysteresis loop obtained with the resistance measurements (R-E) is considerably sharper than the P-E hysteresis loop obtained by the Sawyer-Tower measurement. The rounded nature of the P-E loop is attributable to leakage currents through the PZT layer, which are not present during the measurement of the R-E loop, because no voltage is applied across the ferroelectric during the measurement of the resistance.

We then studied the low-temperature transport properties of these heterostructures. The resistivities for two different PZT/GBCO/PBCO heterostructures as a function of temperature for both polarization states of the PZT layer were measured (13, 14). A shift of the superconducting transition temperature (T_c) of 7 K (Fig. 3, A and B) and switching between superconducting and insulating behavior (Fig. 4) were observed. For Fig. 3A, we measured at room temperature a resistivity change of $\sim 15\%$ upon switching the PZT polarization. As the temperature decreased to ~ 200 K, the resistivities of both curves increased, as did the size of the field effect; this increase can be attributed to the insulating behavior of PBCO. Below 200 K, where the contribution of PBCO to the overall conductivity becomes negligible, metallic behavior was observed, with the size of the field effect increasing to $\sim 50\%$ at the superconducting transition. At the transition, the observed shift in temperature of the two resistivity curves of 7 K was maintained throughout the region of the transition, as demonstrated in Fig. 3B. For the upper curve, the polarization vector points toward the substrate, corresponding to a removal of holes from the *p*-type GBCO that results in a depression of T_c , whereas the lower curve corresponds to an addition of holes to the system. The only difference between these two curves is the state of the ferroelectric polarization. No other modification to the sample was

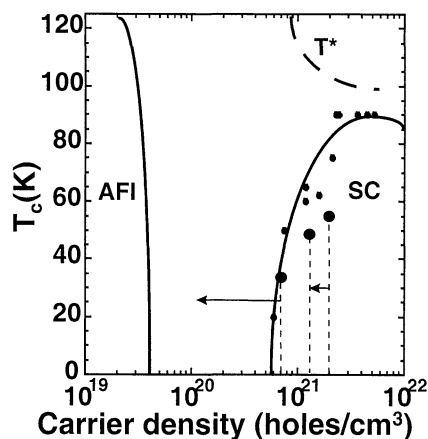


Fig. 1. Schematic temperature-doping phase diagram of the copper oxide superconductors. As the doping level is increased, a transition occurs between an antiferromagnetic insulating state and a superconducting ground state at $T = 0$. T^* is the signature of the pseudogap in these materials. AFI and SC refer to the antiferromagnetic insulating Néel state and the superconducting state, respectively. The small circles are experimental data from (22). Large circles indicate the experimental T_c onset data of this work, and the arrows indicate the shift in carrier density induced by the field effect. The horizontal axis is plotted on a log scale.

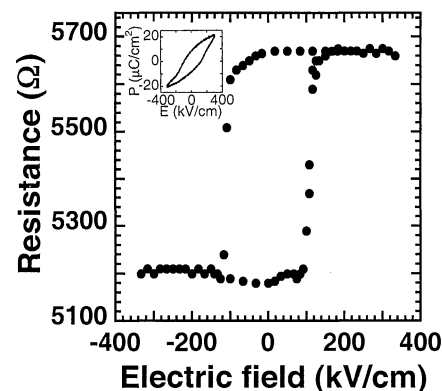


Fig. 2. Ferroelectric hysteresis loop on a 3000 Å PZT/20 Å GBCO/72 Å PBCO heterostructure obtained with resistance measurements (R-E hysteresis). (Inset) A P-E hysteresis loop of this sample obtained through a Sawyer-Tower measurement.

carried out. As with Fig. 2, both states are reversible and nonvolatile.

For the PZT/GBCO/PBCO heterostructure of Fig. 4, the thick lines are measurements taken in zero applied magnetic field, whereas the other curves (below 60 K) are measurements in magnetic fields of 1, 4, and 7 T applied perpendicular to the plane of the film (15). For the lower zero-field curve, the resistivity is essentially temperature-independent from 200 K down to ~50 K, where the onset of the superconducting transition occurs. The resistivity of the sample at this temperature is 2.3×10^{-3} ohm·cm. The application of magnetic fields of up to 7 T has essentially no effect above 50 K, other than the small magnetoresistance that is expected in the normal state of GBCO. Below 50 K, however, the resistive transition broadens substantially with increasing magnetic field because of the motion of field-induced vortices in the superconducting state. At the lowest temperatures and for all the magnetic fields, the transition sharpens.

In contrast, the upper curves, which again correspond to a depletion of holes by the ferroelectric polarization, are insulating throughout the temperature region investigated, except for a dip observed below 20 K. This dip on the insulating side probably occurs because the GBCO thickness is not uniform over the entire film. Atomic force microscopy imaging of the PBCO and GBCO layers reveals the presence of unit cell steps; because of the small Thomas-Fermi screening length in these materials, these thickness variations prevent the polarization field from acting throughout the entire film thickness, leaving regions of the sample that are still superconducting, as confirmed by the sensitivity of the dip to the magnetic field. In addition, within this Thomas-Fermi screening length, there is an exponentially decaying vertical gradient of the carrier concentration. At low temperatures, the insulating behavior is not simply thermally activated. Rather (as shown in the inset to Fig. 4), it can be fitted to variable range hopping (VRH), as well as to the $\ln(1/T)$ behavior that has been observed by Ando and co-workers in their high magnetic field experiments on $\text{La}_{2-x}\text{Sr}_x\text{CuO}_4$ (LSCO) (2, 16). Although the limited temperature range of inves-

tigation precludes a definitive determination based on the fits alone, the density of localized states deduced from the fit to VRH is unphysically large ($\sim 10^{24}/\text{cm}^3$, assuming a tunneling length of 10 Å), which implies that it is not the appropriate conduction mechanism to consider here. As shown in recent magnetic field experiments on $\text{Pr}_{2-x}\text{Ce}_x\text{CuO}_4$, measurements to lower temperatures (<100 mK) are important to more completely address the nature of the insulating state (4).

To quantify the ferroelectric field effect, we have carried out Hall effect measurements to determine the sign and carrier concentration of these films (17). For samples such as the ones shown in Fig. 4, we measure a low-temperature carrier density of $\sim 7 \times 10^{20}$ holes per cubic centimeter, which is below the optimally doped value of $\sim 4 \times 10^{21}$ holes per cubic centimeter that we find for thick GBCO films, revealing that these samples are in the underdoped region of the high- T_c phase diagram. Using the measured remnant polarization of 10 μC per cubic centimeter, we see that the polarization field of the ferroelectric is sufficient to remove the carriers from the material and induce an insulating state. For samples such as the ones shown in Fig. 3, we measure a low-temperature carrier density of $\sim 2 \times 10^{21}$ holes per cubic centimeter, and thus one would not expect to be able to induce an insulating state. These results are summarized in Fig. 1, where the data of this work are plotted on the experimental phase diagram obtained by chemical doping. The arrows indicate the expected shift in carrier density due to the polarization field of the ferroelectric.

The shift in the transition temperature (Fig. 3) and the switching between superconducting and insulating behavior (Fig. 4) represent the largest reversible modulation of superconductivity that has been achieved using a field effect. We attribute these results to the ferroelectric field-effect approach taken here, in which the large polarization field of the ferroelectric applied to ultrathin films induces a substantial modulation of the carrier density. Furthermore, because the effect is nonvolatile, with no voltage being maintained across the insulating ferroelectric, it is not susceptible to leakage cur-

rents or nonlinearities in the dielectric properties of the insulator (8). From the point of view of applications, these experiments demonstrate a route to fabricating a nonvolatile, reversible superconducting switch.

On the theoretical side, we note that the copper oxide superconductors are distinct from the elemental superconductors in that they possess a small superfluid density, which implies that they are sensitive to phase fluctuations as well as to changes in the chemical potential, as evidenced by their temperature-doping phase diagram (Fig. 1). This phase diagram is central to the SO(5) theory of Zhang, in which the antiferromagnetic and superconducting states have a common origin, with their $T = 0$ electronic properties being controlled solely by the chemical potential (5).

Chemical substitution can also be used to change the doping level, and numerous experiments have been performed. However, this approach is often irreversible and alters in an unavoidable and uncontrolled way the microscopic disorder and crystalline structure, which can itself induce a superconductor-insulator transition. The extreme sensitivity of the electronic properties of these materials to even small amounts of Zn substitution that do not modify the doping level is one extreme example of the effect of impurities (3). For the field-

Fig. 3. (A) Resistivity versus temperature of a PZT/20 Å GBCO/72 Å PBCO heterostructure for the two polarization states of the PZT layer. The upper curve corresponds to a removal of holes from the *p*-type GBCO, resulting in an increase in the normal state resistivity and a depression of T_c by 7 K. (B) Expanded view of the data presented in (A). The resistivities ρ of the two curves have been normalized at 100 K.

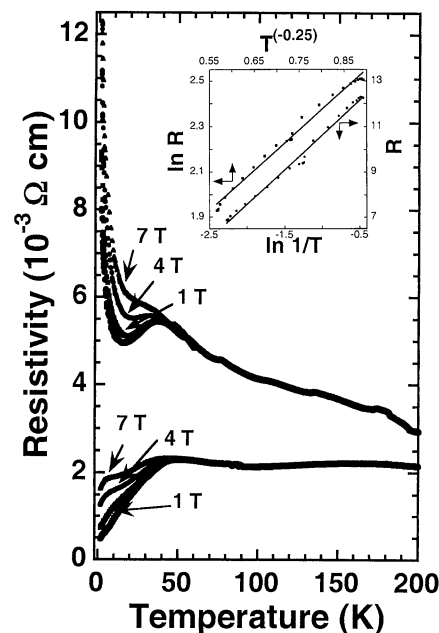
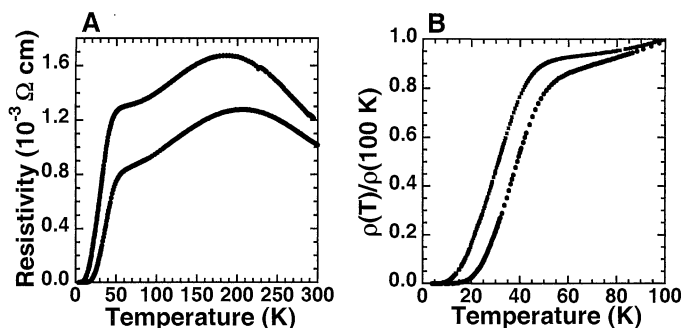


Fig. 4. Resistivity versus temperature of a PZT/20 Å GBCO/72 Å PBCO heterostructure. The upper curves, in which holes have been depleted from the system, are insulating throughout the temperature range investigated, except for a dip below 20 K due to nonuniformities in the field effect. The thick curves are zero field measurements, whereas the other curves are measurements in magnetic fields of 1, 4, and 7 T. (Inset) Fits of the low-temperature insulating behavior to variable range hopping and to $\ln(1/T)$ behavior.

effect approach discussed here, no chemical or structural disorder is introduced, allowing us to identify the key role of the electronic doping level in determining the physical properties of these materials.

In the underdoped superconducting regime, the SO(5) theory of Zhang, as well as the theory of superconductivity in bad metals of Emery and Kivelson, predict that classical and quantum phase fluctuations are responsible for depressing T_c well below the pairing temperature, which, in these theories, is represented by T^* in Fig. 1 (5, 18). As the chemical potential μ is increased, these phase fluctuations decrease because of improved phase stiffness and screening, leading to an increase in T_c . In particular, Emery and Kivelson calculate the T_c dependence for the minimum metallicity required to suppress the phase fluctuations that prevent superconductivity from occurring. This limiting value is nonuniversal and depends on the material, the dimensionality of the system, and the details of the short-range screening. Work on YBCO single crystals, in which radiation damage was used to induce an insulating state, yields a value of $\sim 2.5 \times 10^{-3}$ ohm-cm (19, 20). In this work, we changed the metallicity directly by changing the number of carriers, finding a normal state resistivity of 2.3×10^{-3} ohm-cm. Because YBCO is highly anisotropic and quasi-2D in the underdoped regime, an equivalent 2D sheet resistance, given by the resistivity per copper oxide plane (6Å), is sometimes considered. The equivalent sheet resistance in this case is ~ 40 kohm per square, which is significantly larger than the quantum of resistance for Cooper pairs (6.45 kohm per square).

Finally, regarding the insulating state we observed, the results suggest that because the insulating state is not consistent with variable range hopping, which is what is observed at low doping levels in the antiferromagnetic Néel insulating state up to high temperatures (~ 50 K), the samples may instead be in a quantum disordered state that exists between the Néel and the superconducting ground states (21). The observed $\ln(1/T)$ behavior over the temperature range investigated suggests that this quantum disordered state may also be the state that Ando and co-workers achieved by applying large magnetic fields to underdoped LSCO (2).

References and Notes

1. A. M. Goldman and N. Markovic, *Phys. Today* **51** (no. 11), 39 (1998), and references therein; M. P. A. Fisher, G. Grinstein, S. M. Girvin, *Phys. Rev. Lett.* **64**, 587 (1990); M. P. A. Fisher, *ibid.* **65**, 923 (1990); A. F. Hebard and M. A. Paalonen, *ibid.*, p. 927; Y. Liu *et al.*, *ibid.* **67**, 2068 (1991); A. Yazdani and A. Kapitulnik, *ibid.* **74**, 3037 (1995); E. Chow, P. Delsing, D. B. Haviland, *ibid.* **81**, 204 (1998); S. L. Sondhi, S. M. Girvin, J. P. Carini, D. Shahar, *Rev. Mod. Phys.* **69**, 315 (1997); A. J. Rimberg *et al.*, *Phys. Rev. Lett.* **78**, 2632 (1997); M. I. Erements, K. Shimizu, T. C. Kobayashi, K. Amaya, *Science* **281**, 1333 (1998); G. T. Seidler, T. F. Rosenbaum, B. W. Veal, *Phys. Rev. B* **45**, 10162

- (1992); K. Karpinska *et al.*, *Phys. Rev. Lett.* **77**, 3033 (1996); N. E. Hussey *et al.*, *ibid.* **80**, 2909 (1998).
2. Y. Ando, G. S. Boebinger, A. Passner, T. Kimura, K. Kishio, *Phys. Rev. Lett.* **72**, 4662 (1995); G. S. Boebinger *et al.*, *ibid.* **77**, 5417 (1996).
3. Y. Fukuzumi, K. Mizuhashi, K. Takenaka, S. Uchida, *ibid.* **76**, 684 (1996).
4. P. Fournier *et al.*, *ibid.* **81**, 4720 (1998).
5. S.-C. Zhang, *Science* **275**, 1089 (1997).
6. C. H. Ahn *et al.*, *ibid.* **269**, 373 (1995); Y. Watanabe, *Appl. Phys. Lett.* **66**, 1770 (1995); S. Hontsu, J. Ishii, H. Tabata, T. Kawai, *ibid.* **67**, 554 (1995); S. Hontsu, M. Nakamori, H. Tabata, J. Ishii, T. Kawai, *IEEE Trans. Electron. E80-C*, 1304 (1997); C. H. Ahn *et al.*, *Appl. Phys. Lett.* **70**, 206 (1997); C. H. Ahn *et al.*, *Science* **276**, 1100 (1997); U. Kabasawa, H. Hasegawa, T. Fukazawa, Y. Tarutani, K. Takagi, *J. Appl. Phys.* **81**, 2302 (1997); L. X. Cao *et al.*, *Physica C* **47-52**, 303 (1998).
7. R. E. Glover III and M. D. Sherrill, *Phys. Rev. Lett.* **5**, 248 (1960).
8. J. Mannhart, D. G. Schlom, J. G. Bednorz, K. A. Müller, *ibid.* **67**, 2099 (1991); X. X. Xi *et al.*, *ibid.* **68**, 1240 (1992); A. Walkenhorst *et al.*, *ibid.* **69**, 2709 (1992); J. Mannhart, *Supercond. Sci. Technol.* **9**, 49 (1996).
9. A. W. Kleinsasser *et al.*, *Appl. Phys. Lett.* **55**, 1909 (1989); T. Akazaki *et al.*, *ibid.* **68**, 418 (1996); B. Mayer, J. Mannhart, H. Hilgenkamp, *ibid.*, p. 3031.
10. J.-M. Triscone *et al.*, *J. Appl. Phys.* **78**, 4298 (1996).
11. T. Terashima *et al.*, *Phys. Rev. Lett.* **67**, 1362 (1991); J.-M. Triscone and Ø. Fischer, *Rep. Prog. Phys.* **60**, 1673 (1997).
12. Off-axis scans reveal GBCO [100] (and PBCO [100])||STO [100], as well as epitaxial growth of tetragonal PZT (001) on GBCO (001), with PZT [100]||GBCO [100]. Rocking curves taken around the 005 reflection of PBCO and GBCO have typical full widths at half maximum (FWHM) of $\sim 0.09^\circ$, and rocking curves taken around the 001 reflection of PZT have a typical FWHM of $\sim 0.6^\circ$.
13. Because the primary region of interest is at low temperatures, where PBCO is insulating, the resistivity is calculated using the thickness of the GBCO layer.
14. During fabrication of the heterostructures, the ferro-

- electric layer is uniformly poled. As a result, it was not possible to measure the resistivity for the unpolarized (randomly polarized) state of the ferroelectric.
15. We believe the differences between the samples shown in Figs. 3 and 4 are due to run-to-run variations in the deposition parameters; for example, the substrate temperature and oxygenation of the samples.
16. To suppress the possible influence of the dip, the fits were carried out on the measurements taken at 7 T. Fits to the zero field data, as well as on another sample showing a superconductor-insulator transition in which the dip is not present at zero field, also yield the same conclusions.
17. Because of geometric constraints, it was not possible to measure simultaneously the size of the field effect and the carrier concentration. The Hall effect measurements described in the text were obtained on separate samples showing similar resistivities, critical temperatures, and temperature dependencies.
18. V. J. Emery and S. A. Kivelson, *Phys. Rev. Lett.* **74**, 3253 (1995); *Nature* **374**, 434 (1995). Other theories that consider phase fluctuations include S. Doniach and M. Inui, *Phys. Rev. B* **41**, 6668 (1990); D. Ariosa and H. Beck, *ibid.* **43**, 344 (1991); and T. Schneider and H. Keller, *Phys. Rev. Lett.* **69**, 3374 (1992).
19. A. G. Sun, L. M. Paulius, D. A. Gajewski, M. B. Maple, R. C. Dynes, *Phys. Rev. B* **50**, 3266 (1994).
20. Seidler *et al.*, using a magnetic field as the control parameter, have observed a critical value of 1.6×10^{-3} ohm-cm in underdoped YBCO single crystals [see (1)].
21. M. Kastner, R. J. Birgeneau, G. Shirane, Y. Endoh, *Rev. Mod. Phys.* **70**, 897 (1998); N. W. Preyer *et al.*, *Phys. Rev. B* **39**, 11563 (1989).
22. A. Carrington, A. P. Mackenzie, C. T. Lin, J. R. Cooper, *Phys. Rev. Lett.* **69**, 2855 (1992); T. Ito, K. Takenaka, S. Uchida, *ibid.* **70**, 3995 (1993).
23. We thank M. Beasley, Ø. Fischer, B. Giovannini, Y. Kagan, P. Martinoli, J. Perret, and T. Schneider for useful discussions and D. Chablaix for technical help. Supported by the Fonds National Suisse de la Recherche Scientifique.

19 January 1999; accepted 8 April 1999

Control of Hippocampal Morphogenesis and Neuronal Differentiation by the LIM Homeobox Gene *Lhx5*

Yangu Zhao,¹ Hui Z. Sheng,¹ Reshad Amini,¹ Alexander Grinberg,¹ Eric Lee,¹ SingPing Huang,¹ Masanori Taira,^{2*} Heiner Westphal^{1†}

The mammalian hippocampus contains the neural circuitry that is crucial for cognitive functions such as learning and memory. The development of such circuitry is dependent on the generation and correct placement of the appropriate number and types of neurons. Mice lacking function of the LIM homeobox gene *Lhx5* showed a defect in hippocampus development. Hippocampal neural precursor cells were specified and proliferated, but many of them failed to either exit the cell cycle or to differentiate and migrate properly. *Lhx5* is therefore essential for the regulation of precursor cell proliferation and the control of neuronal differentiation and migration during hippocampal development.

The development of Ammon's horn and the dentate gyrus of the mammalian hippocampal formation is a multistep process controlled by a complex genetic program. During embryonic development, hippocampal precursor

cells originate from the medial wall of the telencephalic vesicles. These cells proliferate in a primary germinal layer called the ventricular zone. Thereafter, they migrate out in a highly organized manner to their appropri-